Available online at www.sciencedirect.com
ScienceDirect
Journal of Catalysis 251 (2007) 374–387
JOURNAL OF CATALYSIS
www.elsevier.com/locate/jcat

Carbon deposited on Ni/Ce–Zr–O isooctane autothermal reforming catalysts

Xiaoyin Chen, Andrew R. Tadd, Johannes W. Schwank *

Transportation Energy Center, Department of Chemical Engineering, 2300 Hayward St., 3014 H.H. Dow Building, University of Michigan, Ann Arbor, MI 48109, USA

Received 7 May 2007; revised 20 July 2007; accepted 27 July 2007

Available online 19 September 2007

Abstract

On-board reforming of liquid fuels is attractive for fuel-cell-powered auxiliary power unit (APU) applications in heavy-duty vehicles. However, a technology barrier is catalyst deactivation due to carbon deposition. In this work, we studied carbon identification and the effect of nickel loading on carbon growth during isooctane autothermal reforming (iC_8-ATR) over Ni-supported Ce–Zr–O (Ni/CZO) catalysts. The crystallographic phase, type, deposition amount, and morphologies of deposited carbon were characterized by X-ray diffraction (XRD), thermogravimetric analysis (TGA), X-ray photoelectron spectroscopy (XPS), and scanning electron microscopy (SEM). Two types of carbon, coating and filamentous, were identified by SEM, with binding energies of 281.6 and 284.5 eV in C1s XPS spectra and oxidation temperatures of 392 and 572 °C in TGA curves, respectively. Both coating and filamentous carbon were X-ray amorphous for nickel loadings $\leqslant$5%, even though deposited carbon reached up to 60.2%. Over the entire nickel loading range of 1–15%, with corresponding nickel crystal sizes of 30–103 nm, the coating carbon formation rates were low (0.04 g/m^2_{Ni} h) and independent of nickel particle size. The growth rates of filamentous carbon increased with increasing nickel particle size. Filamentous carbon growth may require not only a critical nickel particle size, but also a certain minimum number of nickel particles per unit support area. The results suggest a strategy for inhibiting the growth of filamentous carbon on Ni/CZO catalysts during autothermal reforming of liquid fuels.

Keywords: Carbon; Nickel; Cerium zirconium oxide; Isooctane; Autothermal reforming; Thermogravimetric analysis; X-ray photoelectron spectroscopy; Scanning electron microscopy

1. Introduction

The desire for increased fuel economy and decreased CO_2 emissions are two important driving factors in the development of more efficient vehicles that emit less greenhouse gases. Fuel cell vehicles possibly could address these problems, but these have not yet been commercialized. A hybrid system consisting of a conventional internal combustion engine (ICE) for propulsion and a fuel cell-powered auxiliary power unit (APU), which replaces the ICE under heavy NO_x and CO emissions conditions (low speed and idling operations), could be a promising choice due to higher energy efficiency and lower emissions [1]. The APU is a combination of a fuel cell and an on-board hydrogen generation system using gasoline or diesel fuel. Catalytic autothermal reforming (ATR) is an attractive option for hydrogen generation due to its low cost, simplicity, and better energy efficiency compared with steam reforming or partial oxidation. Unlike proton-exchange membrane (PEM) fuel cells, in which CO acts as an anode catalyst poison and thus water–gas shift and preferential oxidation units are required, solid oxide fuel cells (SOFCs) can operate with mixtures of H_2 and CO and are of interest to the military and the trucking industry for on-board fuel cell-powered APU applications. Nickel-based catalysts have been the catalyst of choice for steam reforming to produce hydrogen due to their good activity and long-term stability [2]. The formation of carbon deposits during reaction, however, is one of the main causes of catalyst deactivation during hydrocarbon reforming. Sulfur is also a catalyst poison and is present in many fuels, but may not be a major problem in the future as sulfur-free or very low sulfur fuels become available. Unlike sulfur, carbon deposition is a problem caused by intrinsic properties of the catalyst (e.g., structure, formulation,

* Corresponding author. Fax: +1 734 763 0459.
E-mail addresses: xychen@umich.edu (X. Chen), atadd@umich.edu (A.R. Tadd), schwank@umich.edu (J.W. Schwank).

0021-9517/$ – see front matter
doi:10.1016/j.jcat.2007.07.031

preparation), but can be controlled to some extent by reaction conditions (e.g., type of fuel, steam to carbon ratio, oxygen to carbon ratio, temperature).

Extensive studies have been devoted to carbon deposition during methane reforming on nickel-based catalysts. The main foci have been the identification of carbon type and morphology, nucleation and growth mechanisms, the influence of reaction conditions and catalyst structure, and modifications to reduce carbon formation. Graphitic carbon on a nickel surface was first reported by Dent et al. [3]. Rostrup-Nielsen et al. identified carbon deposits on nickel catalysts in form of filaments [4], and subsequent studies confirmed this observation [5–8]. Additional studies have revealed a variety of types, morphologies, and chemistries of carbon deposited on nickel catalysts depending on the reaction conditions and carbon sources used [2,6,9–12]. The generally accepted mechanism for carbon filament formation is bulk diffusion of carbon through nickel particles to form metastable carbide intermediates at the end of the filaments [2,6,7,11,13,14]; however, an alternative mechanism for the growth of filamentous carbon, via surface diffusion of carbon to the edges of nickel particles, has been demonstrated recently [15–18].

Studies of the relationship between carbon deposition and catalyst structure during hydrocarbon reforming have revealed that support modification and nickel crystallite size have significant effects on carbon formation [17,19,20]. Other efforts have investigated the improvement of carbon resistance by modifying the surface structure of Ni-based catalysts, using additives to form alloys [2,17,21–26] or to promote surface properties [27–29]. Sulfur passivation also has been demonstrated to inhibit the rate of carbon formation more than the rate of reforming [30]. Alloying is thought to inhibit carbon accumulation by decreasing the carbon deposition rate or increasing the carbon gasification rate [13,31]. Bulk carbon is not formed when the gasification rate is greater than the deposition rate [32]. Density functional theory (DFT) has shown that on a Ni–Sn alloy, the barrier to C–O bond formation (i.e., carbon gasification) is lower than the barrier for C–C bond formation (i.e., carbon deposition), in contrast with monometallic nickel, for which the two barriers are about the same [26]. Another method for inhibiting carbon formation is the use of basic supports or basic metal oxide promoters [2,33,34]. Commercial methane-reforming catalysts, in fact, are promoted by the addition of alkali and alkali earth, although this results in a decrease of reforming activity [2]. Recent efforts have been made to minimize carbon formation using rare earth oxides, especially CeO_2, as additives or catalyst supports [21,35,36]. The pronounced resistance of CeO_2 to carbon formation is attributed to improved carbon gasification rates [37–39]. In addition, in a methane dry-reforming study, nickel supported on mixed Ce–Zr–O proved beneficial for suppressing the formation of inactive carbon deposits [40].

The use of hydrocarbons heavier than methane presents an increased risk of carbon formation [41]. Due to the motivations discussed above, however, considerable attention has recently been paid to hydrogen production from liquid fuels via ATR [42] both for distributed electricity generation [43] and on-board vehicle applications [35,44,45]. Pt/CeO_2 is an active catalyst and shows robust resistance to carbon formation during ATR of liquid fuels [35,46,47]. Because platinum is expensive, ceria has poor thermal stability, and zirconia shows a high ability to inhibit carbon formation by promoting the gasification rate [48], a catalyst based on nickel- and zirconia-stabilized ceria should be promising for liquid fuel ATR [44,45,49]. But deactivation due to carbon deposition is a problem that still must be solved for the nickel-supported ceria–zirconia system, particularly at high nickel loadings [50]. Although a great deal about carbon formation during methane reforming has been learned, it remains to be seen whether the principles and strategies developed to reduce carbon deposition in that system can be applied to the reformation of liquid fuels. To prevent deactivation due to carbon deposition [26,45,50], it is necessary to identify the types of carbon formed and the relationship of carbon deposition and nickel loading. The current work presents a combined identification and characterization of carbon deposited on nickel-based ceria–zirconia catalysts of different nickel loadings during isooctane ATR. One of the objectives is to distinguish between carbon overlayers ("coating carbon") and filamentous carbon; however, it is not the purpose of this work to study the detailed nature of nanotubes, such as identification of single-walled versus multiwalled nanotubes.

2. Experimental

2.1. Preparation of fresh NiO/Ce–Zr–O

The ceria–zirconia mixed oxide (CZO) with a composition of $Ce_{0.75}Zr_{0.25}O_2$ was synthesized by coprecipitating a mixed aqueous solution of $Ce(NO_3)_3$ and $ZrOCl_2$ salts using ammonium hydroxide as a precipitating agent. The precipitate was recovered by filtration and washed with deionized water, dried at 110 °C, and finally calcined at 600 °C in air for 2 h. Nickel oxide supported on CZO (NiO/CZO) with different nickel loadings was prepared by incipient wetness impregnation using an aqueous solution of nickel nitrate. After impregnation, the catalyst was dried at 110 °C and calcined at 600 °C in air for 1 h.

2.2. Autothermal reforming and carbon deposition

Carbon deposition was carried out during ATR of isooctane (iC_8-ATR) using approximately 80 mg of catalyst mixed with 240 mg of silica gel. The silica gel was calcined at 850 °C in air before use and was of the same particle size as the catalyst (60–80 mesh). The catalyst and diluent mixture was loaded into a $\frac{1}{2}$-inch-diameter quartz reactor tube and reduced in situ at 600 °C under a flow of 350 ml/min of 5% H_2 in N_2. The reduced catalyst, Ni/CZO, is designated *xx*Ni/CZO, where *xx* represents the weight percent nickel loaded on CZO, as shown in Table 1.

Various iC_8-ATR operations were run over Ni/CZO catalysts under different reaction protocols to investigate catalyst deactivation due to carbon deposition [50]. As shown in the iC_8-ATR protocol in Fig. 1, the reaction procedure in this work was started at 300 °C using a fuel flow rate of ∼0.14 g/min,

Table 1
Physicochemical properties of NiO/CZO and Ni/CZO

Sample	Ni (wt%)	NiO/CZO[a]			Ni/CZO[c]			
		BET (m^2/g)	Average grain size[b]		Dispersion (%)	Ni surface area		Particle size (nm)
			NiO (nm)	CZO (nm)		(m^2/g_{cat})	(m^2/g_{Ni})	
1Ni/CZO	1	57	n.d.	13.4	3.1	0.21	21	33
2Ni/CZO	2	53	n.d.	13.1	3.4	0.45	23	30
5Ni/CZO	5	43	12.6	12.6	2.7	0.90	18	38
					3.2[d]	1.07	21	32
					2.6[e]	0.86	17	39
10Ni/CZO	10	42	20.9	12.7	1.6	1.04	10	65
					1.6[d]	1.08	11	62
15Ni/CZO	15	44	31.1	12.4	1.0	0.99	7	103

[a] Fresh NiO/CZO after calcining $Ni(NO_3)_2$/CZO at 600 °C in air.
[b] Estimated by Scherrer's equation from XRD patterns.
[c] Estimated from CO chemisorption after 600 °C reduction by H_2 flow.
[d] Estimated from H_2 chemisorption after 600 °C calcination.
[e] Estimated from H_2 chemisorption after 650 °C calcination.

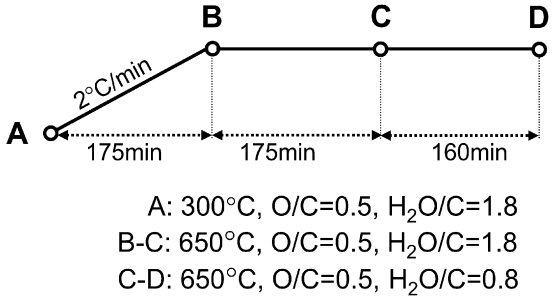

Fig. 1. iC_8-ATR protocol over Ni/CZO catalysts.

an O/C ratio of 0.5, a H_2O/C ratio of 1.8, and 500 ml/min of argon (GHSV = 700,000 h^{-1}), with the furnace ramped to 650 °C at a rate of 2 °C/min and held at 650 °C for 175 min. Then the H_2O/C ratio was decreased to 0.8, and the argon flow was stopped, to create severe conditions conducive to carbon deposition. The catalyst was held under these conditions for another 160 min. The reactant flow was then stopped and replaced with nitrogen while the reactor was cooled to room temperature. A blank run following the same procedure was carried out using only silica gel. Reaction products were passed through a stainless cold water condenser and then through a knockout vessel positioned in an ice bath to collect excess water and unreacted hydrocarbons. After the knockout, gas products were analyzed by an online gas chromatograph (Varian CP-3800) equipped with a thermal conductivity detector using argon carrier and a 10-ft Carbosphere 1000 packed column (Alltech). Molar fractions Y of H_2, O_2, N_2, CO, CH_4, and CO_2 in the product were determined. Isooctane conversion (X_{iC_8}) was calculated using the gas-phase-containing products, CO, CH_4, and CO_2, according to the following formula [45]:

$$X_{iC_8} = \frac{F_{N_2,in} \cdot (Y_{CO} + Y_{CO_2} + Y_{CH_4})_{out}}{Y_{N_2,out} \cdot (8 \cdot F_{iC_8H_{18},in})}.$$

Accordingly, the H_2 yield was represented by

$$Y_{H_2} = \frac{F_{H_2,out}}{9 \cdot F_{iC_8H_{18},in}}.$$

In the foregoing equations, F represents the molar flow rate of the subscripted species in mol s^{-1}.

2.3. Regeneration of spent catalyst after iC_8-ATR

After iC_8-ATR, the spent catalyst samples (Ni/CZO and SiO_2) were regenerated at 600 °C by oxidation under flowing dry air for 1 h, flushing with nitrogen for 15 min, and then reduction under 5% H_2/N_2 for 2 h.

2.4. Catalyst characterization

The BET specific surface areas of the fresh catalysts (NiO/CZO) were measured using nitrogen physisorption at −196 °C using a Quantachrome CHEMBET-3000. CO and H_2 chemisorptions were carried out to determine metal nickel dispersion, nickel surface area, and nickel crystallite size using a Quantachrome CHEMBET-3000 and a Micromeritics ASAP 2020, respectively. For CO chemisorption, the calcined samples were degassed at 350 °C under a N_2 flow for 2 h, and then reduced in situ under a 30% H_2/N_2 flow of 80–100 ml/min at 600 °C for 1 h before CO pulse chemisorption at 35 °C. For H_2 chemisorption, the samples were reduced in situ under a H_2 flow of 60–80 ml/min at 600 °C for 2 h, after which the analysis procedure was conducted. The H_2 chemisorption data were collected at 35 °C. The metal dispersion was calculated by assuming an adsorption stoichiometry of one CO molecule or one H atom per one exposed nickel atom. Powder X-ray diffraction (XRD) was used to identify the crystallographic phases of fresh and spent catalyst samples. XRD experiments were carried out on a Rigaku rotary anode instrument using Cu$K\alpha$ radiation at 40 kV and 100 mA. To characterize carbon–hydrogen bonds of carbon deposits, the infrared spectrum of the spent catalyst was collected from samples pressed into a KBr pellet in a Perkin–Elmer FT-IR SPECTRUM 2000. Temperature-programmed oxidation (TPO) of carbon present on spent catalysts was performed under dry air flow in a Perkin–Elmer TGA-7 thermogravimetry analyzer (TGA) coupled to a Perkin–Elmer FT-IR SPECTRUM

2000 (KBr optics) for characterization of evolved gases. The TGA heating ramp ($R = 10\,^{\circ}C/min$) was synchronized with the FTIR (3.6 s/scan). The spectra of evolved gases were collected using TimeBase software in the range of 450–4000 cm^{-1}.

X-ray photoelectron spectroscopy (XPS) was performed on the fresh and spent catalysts to characterize the status of different types of carbon species deposited on Ni/CZO using a Kratos Axis Ultra XPS analyzer. Samples post isooctane ATR were ground into powder form and then pressed onto the surface of 0.25-mm-thick indium foils. Before XPS analysis, the samples were evacuated in the sample chamber for at least 4 h until a pressure $\leqslant 5 \times 10^{-7}$ Torr was reached, then transferred into the analysis chamber, where they were evacuated at $\leqslant 5 \times 10^{-9}$ Torr overnight. The XPS was operated using a mono-aluminum source at 10 mA and 15 kV. The choices of scan number and pass energy for individual elements were based on element surface concentration and signal intensity (count per second [cps]); for example, a pass energy of 20–40 eV and 40–80 scans were applied for adventitious carbon (C1s) scanning on fresh NiO/CZO samples, compared with a pass energy of 10 eV and 60–100 scans for C1s scanning of carbon-deposited catalysts. A pass energy of 40 eV was used for Ni2p and Zr3d scanning for both the fresh and carbon-deposited catalysts. During XPS spectra acquisition, the sample charge neutralizer was activated, to eliminate surface charging for electrically nonconductive samples. All binding energies of XPS spectra found in this work are reported as raw data with no correction relative to adventitious carbon (which normally is adjusted to 284.5 eV), to facilitate the comparison of adventitious carbon and deposited carbon species.

Scanning electron microscopy (SEM) imaging of the fresh and spent catalyst morphology was carried out and compared using a FEI Nova Nanolab and a Philips XL30FEG instrument. Energy-dispersive X-ray spectroscopy (EDS) microanalysis performed on an EDAX system was coupled with the SEM for surface elemental analysis. The SEM was done at 10–15 kV and 0.14–0.58 nA, depending on the surface charging of the samples. The SEM specimen preparation was varied depending on electrical conductivity of the samples. Unless otherwise noted, the specimens were typically prepared by loading the ground catalyst onto an Al–Mg alloy holder without Au coating.

3. Results

3.1. Surface area, crystallographic phase, and nickel dispersion of catalysts

The physicochemical properties of fresh NiO/CZO and reduced Ni/CZO catalysts with different nickel loadings are listed in Table 1. The specific surface area of synthesized CZO after calcination at 600 °C was 60 m^2/g. Adding nickel at 1 and 2% decreased the catalyst surface area by 5 and 12%, respectively. Increasing the nickel loading to 5% decreased the surface area by 28%, to 43 ± 1 m^2/g, but further increases in nickel loading up to 15% did not change the surface area any further. The average grain size of CZO as determined from an XRD line-broadening analysis was about 13 nm. Fig. 2 shows the XRD patterns of fresh NiO/CZO, which are in good agreement with published patterns of $Ce_{0.75}Zr_{0.25}O_2$ (PDF 00-028-0271). Two additional weak peaks can be seen at 43.3° and 37.3° corresponding to (012) and (101) reflections of nickel oxide. After reduction in hydrogen, these two additional peaks appeared at 44.5° and 51.8°, corresponding to the (111) and (200) reflections of metallic nickel (PDF 00-004-0850).

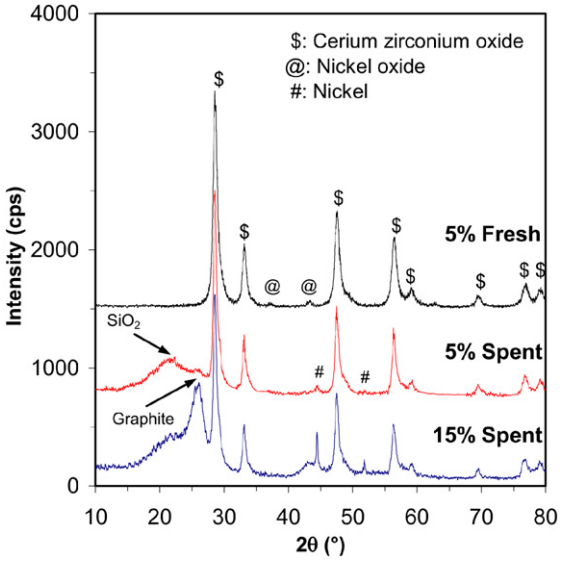

Fig. 2. XRD patterns of fresh NiO/CZO (5% Ni) and spent Ni/CZO catalysts with Ni loading of 5% and 15% following iC_8-ATR.

The nickel particle size as measured from CO chemisorption was 30–33 nm for nickel loadings in the range of 1–2% but grew to 38, 65, and 103 nm as nickel loading was increased to 5, 10, and 15%, respectively, indicating that the nickel dispersion decreased with increasing nickel loading. If, for arguments sake, the nickel dispersion of all samples was assumed to be 3.1% (the dispersion level observed for the 1% Ni sample), then the expected metal nickel surface area would be 0.21, 0.42, 1.05, 2.10, and 3.15 m^2/g_{cat} for nickel loadings of 1, 2, 5, 10, and 15%, respectively. However, the actually measured surface areas of metallic nickel were much lower: 0.21, 0.45, 0.90, 1.04, and 0.99 m^2/g_{cat}, corresponding to 21, 23, 18, 10, and 7 m^2/g_{Ni}, respectively.

There were three regimes of nickel loading on CZO: (1) in the nickel range of 1–2 wt%, doubling the nickel loading roughly doubled the nickel surface area, because the nickel particle size was maintained at the same level due to abundant surface area of CZO; (2) in the range of 2–10%, additional nickel increased the total metal surface area, but the increase was no longer linear because the particle size also increased; and (3) going from 10 to 15% nickel loading, the metal surface area remained nearly constant due to the decreased nickel dispersion and the increased particle size. This indicates that the nickel particles are growing at high metal loadings, probably due to a lack of unoccupied sites on the CZO support. The variations in BET surface area, nickel particle size, and surface area with changes in loading suggest that at low loading, the NiO precursor derived from $Ni(NO_3)_2$ impregnation was

located preferentially inside the pores of CZO aggregates, restricting the final size of the metal crystallites. As more nickel was added, the NiO precursors required more than the available pore space and started to deposit on the external surface. Once this point was reached, there was no further increase of metal surface area on CZO with increasing nickel loading. The size of the nickel particles outside of the CZO pores was unrestricted, and these particles were free to grow as the nickel loading was increased, resulting in the observed increased in nickel particle size from 30 to 103 nm. It should be noted that the so-called "pores" of the support CZO resulted from packing together CZO aggregates of different sizes, with each aggregate composed of many smaller (∼13 nm) CZO crystallites. During catalyst preparation by impregnation, these pores filled with $Ni(NO_3)_2$ precursor, and upon calcination, NiO was distributed on the internal surface of these pores.

H_2 chemisorption was also carried out on 5Ni/CZO and 10Ni/CZO catalysts after calcination and H_2 reduction at 600 °C to compare the nickel dispersion obtained from CO chemisorption. The nickel particle sizes were 32 nm for 5Ni/CZO and 61 nm for 10Ni/CZO, consistent with the CO chemisorption results (Table 1).

3.2. Autothermal reforming and carbon deposition

Autothermal reforming is a complex combination of steam reforming and partial oxidation, with some contributions from the water–gas shift. It is still not clear whether the carbon formation during iC_8-ATR is a byproduct of the steam-reforming reaction or the partial oxidation pathway; nonetheless, we do know that carbon formation is dependent on catalyst formulation and reaction conditions, such as temperature, O/C ratio, and H_2O/C ratio [50]. Higher temperature and higher O/C and H_2O/C ratios favor decreased carbon formation. Once the reaction temperature is fixed, deactivation due to carbon formation depends mainly on the concentration of iC_8 in the feed stream and on the ratios of O/C and H_2O/C. Extensive investigations of iC_8-ATR over Ni/CZO catalysts revealed only minimum carbon deposition under the reaction conditions of stages A–C in Fig. 1. As the reaction temperature increased from 300 to 650 °C with O/C = 0.5 and H_2O/C = 1.8, as shown in Fig. 3, both the extent of isooctane reformation (i.e., the iC_8 conversion to CO_x [CO and CO_2] and CH_4) and the hydrogen yield increased. Higher nickel loadings gave higher conversion and hydrogen yields, because nickel was the active site for iC_8 conversion and H_2 production. During stages B and C, at 650 °C with O/C ratio of 0.5 and an H_2O/C ratio of 1.8, the catalysts with nickel loadings ⩾10% showed decreases in both iC_8 conversion and H_2 yield, whereas the catalysts with nickel loadings ⩽5% showed no evidence of deactivation for both iC_8 conversion and H_2 yield, in agreement with iC_8-ATR on the Pt/Ce–Zr–O catalyst [44]. On decreasing the H_2O/C ratio to 0.8 and cutting out the Ar flow (stages C and D in Fig. 1), the catalysts with nickel loadings ⩾5% showed mild decreases of iC_8 conversion, whereas those with nickel loadings ⩽2% demonstrated stable iC_8 conversion. All

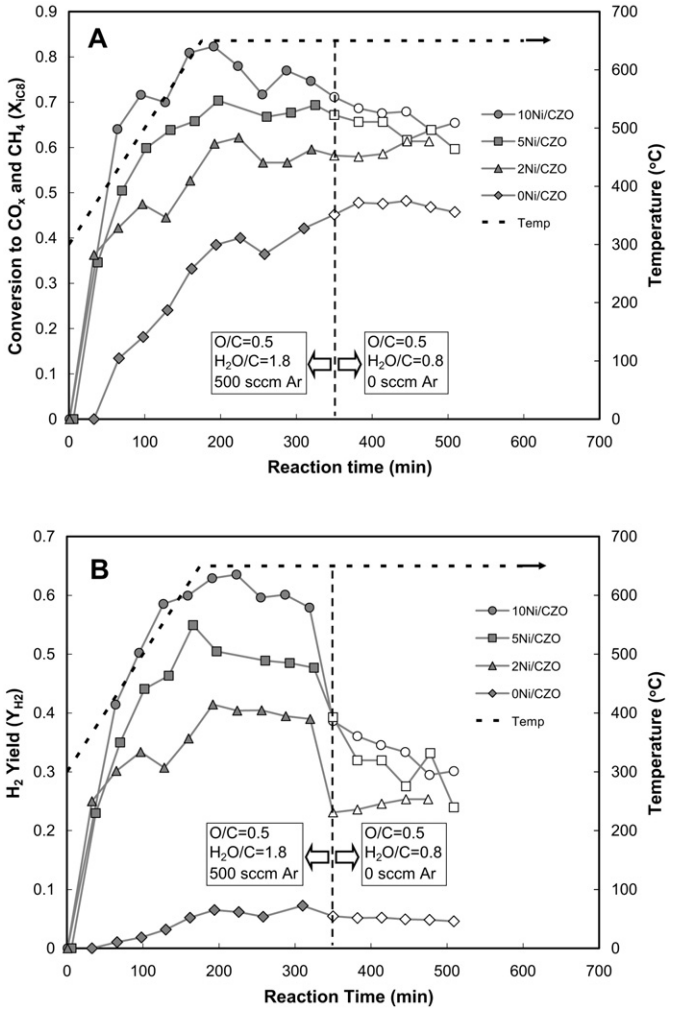

Fig. 3. Comparison of iC_8 conversion (A) and hydrogen yield (B) under different reaction stages of iC_8-ATR over Ni/CZO catalysts with different nickel loadings.

of the Ni-containing catalysts exhibited a sharp decrease in H_2 yield.

As shown in Fig. 3, the support Ce–Zr–O by itself is an active oxidation catalyst for isooctane. Related work in our laboratories on monolith-supported nickel/CZO catalysts (not shown) showed that Ce–Zr–O oxide can also act as an oxidation catalyst for dodecane.

The catalyst series used in this study were characterized after calcination at 600 °C, because they were originally intended for use in an iC_8-ATR study at 600 °C. In the course of the present carbon deposition study, we evaluated carbon deposition at reaction temperatures of 500, 600, and 650 °C. As mentioned above, a reaction temperature of 650 °C was better for H_2 yield and iC_8 conversion without excessive carbon deposition under the ATR conditions of O/C = 0.5 and H_2O/C = 1.8. However, as can be seen from the additional data in Table 1, calcining the catalyst at 650 °C did not change the Ni particle size significantly. After calcining the 5Ni/CZO catalyst at 650 °C for 1 h, H_2 chemisorption showed a Ni particle size of 39 nm, close to the particle size obtained after calcination at 600 °C.

3.3. Deposited carbon characterization by FTIR, TGA, XRD, and XPS

FTIR framework vibration analysis using a KBr pressed pellet of the spent 5Ni/CZO catalyst exhibited no evidence of C–H bonds. Furthermore, during TPO of spent catalysts analyzed by TGA-IR, the IR spectra of evolved gases showed no water peaks in the range of 1340–1860 cm^{-1} even for the spent 15Ni/CZO catalyst with 88% of deposited carbon.

The total amount of carbon deposited on the spent catalysts and the peak temperature of oxidation were determined by TGA. Fig. 4 shows the derivative thermal gravimetric (DTG) change versus temperature and the integrated intensity of the evolved CO_2 band versus temperature obtained from online IR spectra. At 1% nickel loading, only a low-temperature peak at 392 °C (carbon T_{392}) was observed in the DTG curves. Increasing the nickel loading to 2% produced a second high-temperature peak at 572 °C (carbon T_{572}). The presence of two TGA peak temperatures indicates that two different types of carbon were deposited. The peak intensity of carbon T_{392} and the peak position of carbon T_{572} did not change as the nickel loading increased, but the higher the nickel loading, the more carbon was deposited in the carbon T_{572} form, as shown by the DTG and FTIR results. The approximate 6 °C difference between the peak temperatures observed in TGA and FTIR can be attributed to the flow delay between the TGA and FTIR sample cell.

Quantitative estimation of deposited carbon from thermogravimetric curves, as shown in Table 2, was done by calculating the weight loss at 250–440 °C for carbon T_{392} and 440–700 °C for carbon T_{572}. In the samples diluted with silica, the total amount of carbon deposited during iC_8-ATR ranged from 1.6–64.7 wt% over the nickel loading range of 1–15%. No carbon deposition was observed when silica alone was used under iC_8-ATR conditions. The changes in the carbon deposition, corrected by subtracting the weight of diluent silica, were much greater than the changes in nickel loading. The distribution of carbon mass between T_{392} and T_{572} types was also dependent on the nickel loading. Most of the carbon on 1Ni/CZO was carbon T_{392}. The quantity of carbon T_{572} increased significantly as the nickel loading increased.

Table 2
Quantified deposited carbon measured by TGA-IR

Sample	Carbon T_{392}				CO_2 peak	(°C)
	Total	wt%-C	wt%[a]	Ratio (%)		
1Ni/CZO	1.6[a]	6.6[b]	1.1	70	398	
2Ni/CZO	3.1[a]	12.6[b]	1.2	40	398	577
5Ni/CZO	27.4[a]	60.2[b]	3.1	11	398	577
10Ni/CZO	39.8[a]	72.6[b]	1.4	3	n.d.	577
15Ni/CZO	64.7[a]	88.0[b]	1.3	2	n.d.	577

[a] Measured by catalyst–diluent (SiO_2) mixture.
[b] Corrected by subtracting the weight of diluent SiO_2.

XRD was performed on the spent Ni/CZO catalysts for crystallographic-phase characterization of deposited carbon species. Fig. 2 shows the XRD patterns of the spent 5Ni/CZO and 15Ni/CZO catalysts. Note that the broad peak at 2θ of 20–25° in Fig. 2 reflects the diffraction of silica diluent. For the catalysts with >5% Ni loading, two weak peaks besides those of CZO were observed at 44.5° and 51.8° that are indicative of metallic nickel. Surprisingly, no peaks indicative of nickel carbide and only a very small peak corresponding to graphite reflections were found on 5Ni/CZO, even though the carbon deposition reached 60.2 wt%. But a strong graphite peak was observed for the 15Ni/CZO sample, with the amount of carbon deposition increasing to 88.0 wt%. In this case, very strong metallic nickel peaks were observed, but no evidence of the presence of nickel oxide or nickel carbides was found.

XPS performed to characterize the chemical status of deposited carbon species showed two different carbon-binding energies present that could be attributed to deposited carbon, in agreement with the TGA results. Fig. 5 shows C1s core spectra of fresh 2Ni/CZO (2% NiO/CZO) and spent catalysts in the nickel loading range of 1–5%. Fresh 2Ni/CZO showed a weak (PE = 20 eV) C1s peak at 282.1 eV. This peak can be assigned to adventitious carbon. The adventitious carbon on the sample surface may originate from the atmosphere, sample handling, and the contamination in the XPS chamber. The 1Ni/CZO spent sample showed a strong carbon peak (PE = 10 eV) located at

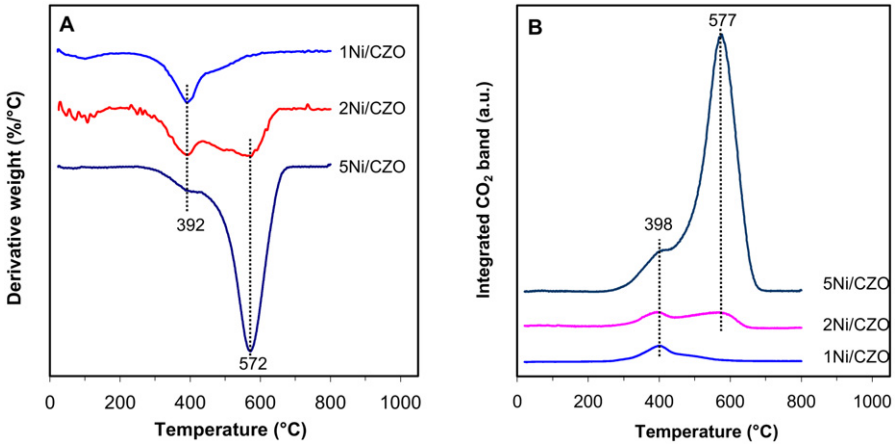

Fig. 4. Derivative thermal gravimetric curves (A) and integrated IR bands of evolved CO_2 (B) of spent Ni/CZO catalysts with different nickel loadings.

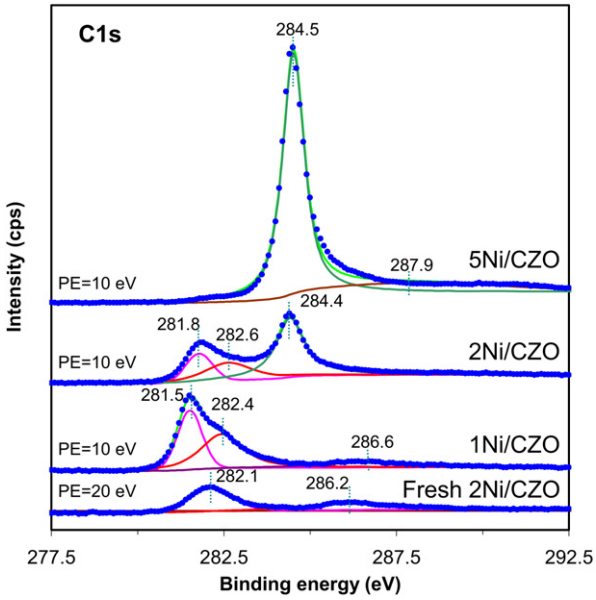

Fig. 5. C1s core spectra of fresh NiO/CZO (2 wt% Ni) and spent Ni/CZO catalysts with different nickel loadings.

281.5 eV and a shoulder peak at 282.4 eV originating from the adventitious carbon. The intensity of the C1s peak at 281.5 eV was stronger than that of the peak at 282.4 eV. The peak at 281.5 eV can be attributed to carbon deposited on Ni/CZO during iC_8-ATR; the spent 2Ni/CZO catalyst showed a similar C1s peak at 281.8 eV when the same pass energy (PE = 10 eV) was applied. The spent 2Ni/CZO catalyst showed adventitious carbon at 282.6 eV and an additional C1s peak at 284.4 eV. The latter C1s peak represents a second type of deposited carbon species. These two XPS C1s peaks assigned to deposited carbon are consistent with the two distinct peak temperatures in TGA. However, the spent catalysts with Ni loadings $\geqslant$5% showed only one strong peak at 284.5 eV and a nonpronounced adventitious carbon peak. On comparison with the spectra of the 2Ni/CZO sample, this single peak can be attributed to the second type of deposited carbon, indicating that the surface of this catalyst was totally covered by the second type of deposited carbon.

It should be pointed out that XPS of Ni2p can be useful in identifying the status of Ni species, including the presence of carbides. However, even for the fresh NiO/CZO (2% Ni loading) sample, only a weak Ni2p signal attributed to NiO was detected. For all postreaction samples with nickel loading in the range of 1–15%, no Ni2p XPS peaks were detectable because of carbon deposition on the surface.

3.4. Carbon deposition characterization by scanning electron spectroscopy

Both TGA-IR and XPS analysis indicated that two types of carbon species, carbon T_{392} and carbon T_{572}, were formed on Ni/CZO during iC_8-ATR. Whereas the amount of carbon T_{392} was independent of nickel loading, the amount of carbon T_{572} was closely related to nickel loading. Graphitic carbon

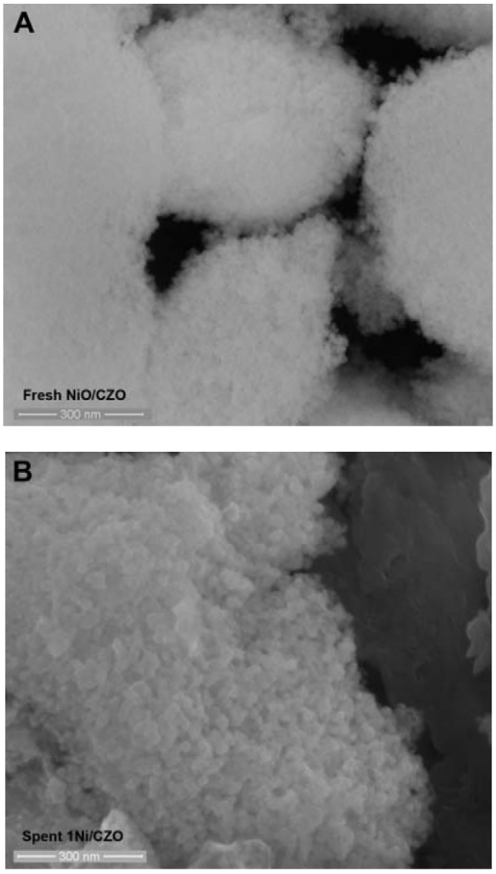

Fig. 6. Comparison of morphological texture of fresh NiO/CZO (2 wt% Ni) (A) and spent 1Ni/CZO (B). The samples were not coated with Au prior to SEM.

was only detected by XRD, however, at very high carbon accumulations (>60.2 wt%). XPS indicated that carbon T_{392} was formed before carbon T_{572}. To gain insight into the nature of deposited carbon and the relationship between carbon formation and nickel loading, we studied the morphologies of these different types of carbon species on the spent catalysts using SEM.

3.4.1. Spent 1Ni/CZO and fresh 2NiO/CZO catalyst

Fig. 6A shows an SEM image of fresh 2% NiO/CZO. Here the estimated precursor size is approximately 20 nm, in good agreement with the crystal size obtained from XRD line-broadening analysis. These precursor particles formed aggregates with 0.1–0.5 μm. Fig. 6B shows an SEM image of spent 1Ni/CZO after iC_8-ATR. Although TGA showed a carbon deposition of 6.6% after iC_8-ATR, it revealed no carbon filaments. But the images of the spent catalyst were much sharper than those of the fresh catalyst. The precursor size also increased to approximately 25 nm. When the fresh 2Ni/CZO and spent 1Ni/CZO were coated with Au before SEM analysis, the images obtained for both samples became much sharper. Clearly, deposition of carbon T_{392} produced an effect similar to Au coating. Thus, it can be inferred that carbon was present as a thin coating layer formed on Ni/CZO under carbon deposition conditions. The effect of this “coating carbon” deposited during

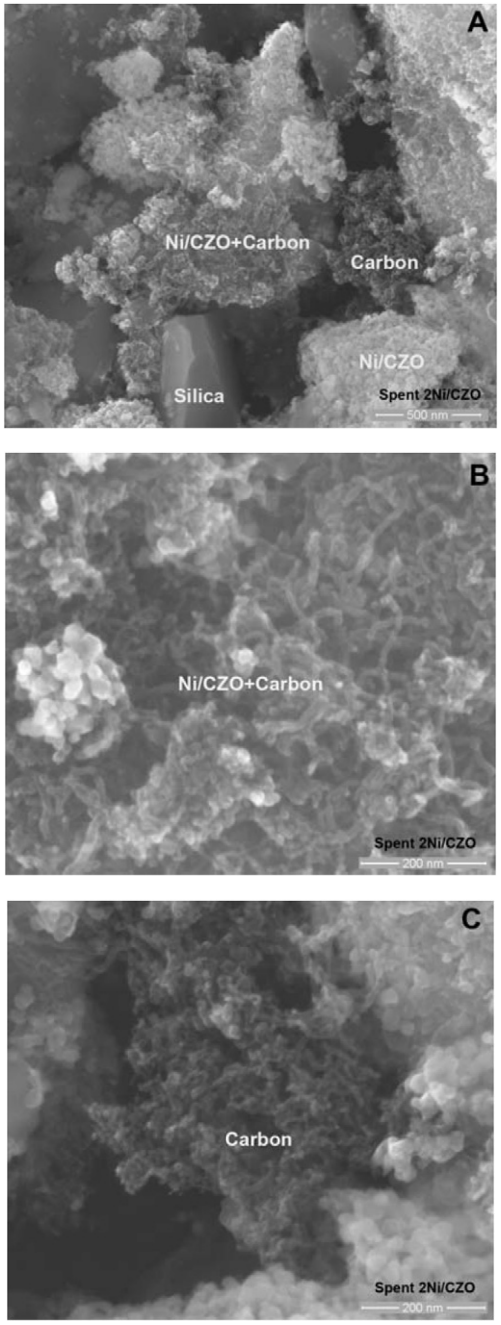

Fig. 7. SEM images of spent 2Ni/CZO catalyst that show different domains.

autothermal reforming is very similar to the effect of carbon sputter-coated to make insulating SEM samples conductive.

3.4.2. Spent 2Ni/CZO catalyst

Filamentous carbon could be readily observed on the 2Ni/CZO catalyst after iC_8-ATR. Examination and scanning of many sample regions revealed four apparent domains on the spent catalyst surface: silica, Ni/CZO, a mixture of Ni/CZO and filamentous carbon, and closely packed carbon filaments (Fig. 7).

TGA analysis showed no weight loss from SiO_2 used under carbon deposition conditions. Elemental microanalysis of the silica domain in 2Ni/CZO showed no carbon, with Si giving the highest-intensity signal (Fig. 8). The texture of this silica domain was smooth (see Fig. 7A). The Al signal observed is due to the sample holder. The atom % composition in this domain, estimated by EDAX ZAF quantification through standardless element normalization, was 59.97% (O), 6.21% (Al), 33.01% (Si), and 0.81% (Ce). The Ni/CZO domain without carbon filaments in the lower right region of Fig. 7A demonstrated a morphology indicative of coating carbon deposition, similar to that of the spent 1Ni/CZO. The particle size in this region was estimated to be 25 nm. Although no filaments were visible, EDS of this domain gave a carbon signal approximately half as intense as that of the Ni/CZO + carbon domain. An enlargement of the Ni/CZO + filamentous carbon region, given in Fig. 7B, shows that these filaments are closely associated with Ni/CZO and are carbon nanotubes approximately 12 nm in diameter. The Ni/CZO precursor particles not covered by filaments have a diameter of approximately 25 nm and form large aggregates. The EDS results for this region, given in Fig. 8, showed an atom % composition of 56.56% (C), 31.23% (O), 2.23% (Al), 2.16% (Si), 1.59% (Zr), and 6.23% (Ce). These results indicate the presence of two types of carbon with different morphologies on the spent Ni/CZO catalyst. In addition to carbon filaments growing on Ni/CZO, other domains containing only carbon filaments also were observed, as shown in Fig. 7C.

An attempt was made to explore the relationship between the two types of carbon. Fig. 9 presents an SEM image of 2Ni/CZO after iC_8-ATR. This image shows clearly distinguishable domains of coating carbon and filamentous carbon on a single Ni/CZO aggregate. The coating carbon morphology is similar to that observed on spent 1Ni/CZO. The ratio of X-ray counts per second (cps) of the coating carbon region to the filamentous carbon region is about 1.60. This is close to the ratio of the weight loss of the carbon T_{392} and carbon T_{571} (1.63) reported in Table 2. Based on inspection of Fig. 9, it seems possible that carbon might be first deposited as coating carbon and then transformed to the filamentous form if both types are associated with nickel, but the evidence of this is not yet conclusive.

3.4.3. Spent 5Ni/CZO catalyst

Fig. 10 shows the SEM images and EDS microanalysis obtained for 5Ni/CZO after iC_8-ATR. In the SEM image, silica has a smooth texture and thus can be clearly distinguished from spent Ni/CZO. EDS of the silica domains revealed no carbon deposits. Significant carbon deposits in the form of filaments were observed in the Ni/CZO domain. This is consistent with the increased mass of carbon T_{572} found during TGA (Fig. 4; Table 2). Fig. 10B shows these carbon nanotubes with an average diameter of 12 nm. This is the same average diameter found at lower nickel loadings. EDS results showed very strong carbon signals, with a carbon-to-cerium ratio of about 58, compared with 3.6 in similar domains on the spent 2Ni/CZO shown in Fig. 7C. Taken together, these results confirm that the T_{572} species is filamentous carbon and that its deposition is dependent on nickel loading.

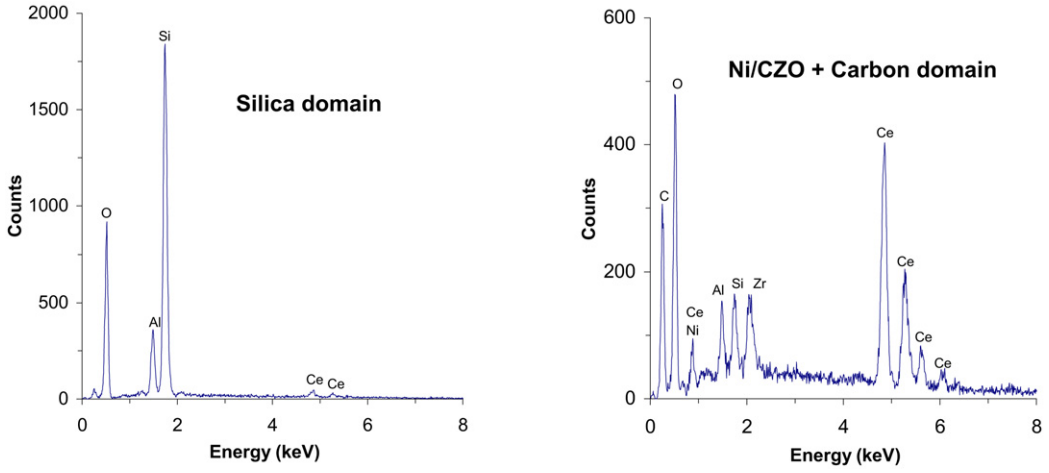

Fig. 8. Typical energy dispersive X-ray spectroscopy (EDS) of different domains of spent 2Ni/CZO catalyst. EDS was performed on a Philips XL30FEG scanning electron microscope with EDAX.

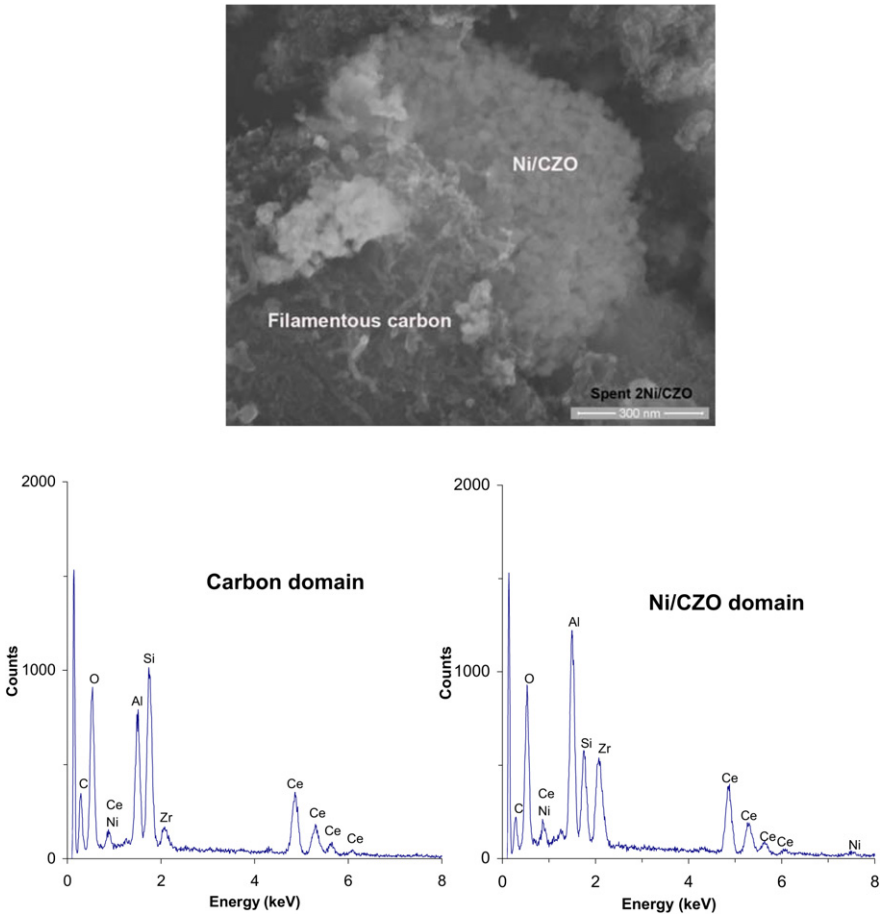

Fig. 9. SEM image of spent 2Ni/CZO catalyst with EDS analysis of filamentous carbon and Ni/CZO domains.

3.4.4. Regeneration of Ni/CZO catalyst

The deposited carbon was removed by exposure to oxygen at elevated temperature. Fig. 11 shows the SEM image of spent 5Ni/CZO that was oxidized and then reduced at 600 °C under 5% H_2/N_2. The particles composing the larger aggregates were close in size to the particles of the freshly prepared catalyst before iC_8-ATR, with no obvious sintering. The images obtained were sharper than in the fresh sample, indicating that the metallic nickel decreased surface charging. As mentioned above, no significant nickel particle size change was observed from H_2 chemisorption on comparing the 5Ni/CZO catalyst after treatment for 1 h at 600 and 650 °C, respectively. Supporting evidence indicating that going from 600 to 650 °C did not significantly change the Ni particle size came from a systematic comparison of the influence of calcination temperature on nickel particle size in a similar catalyst system. H_2 chemisorp-

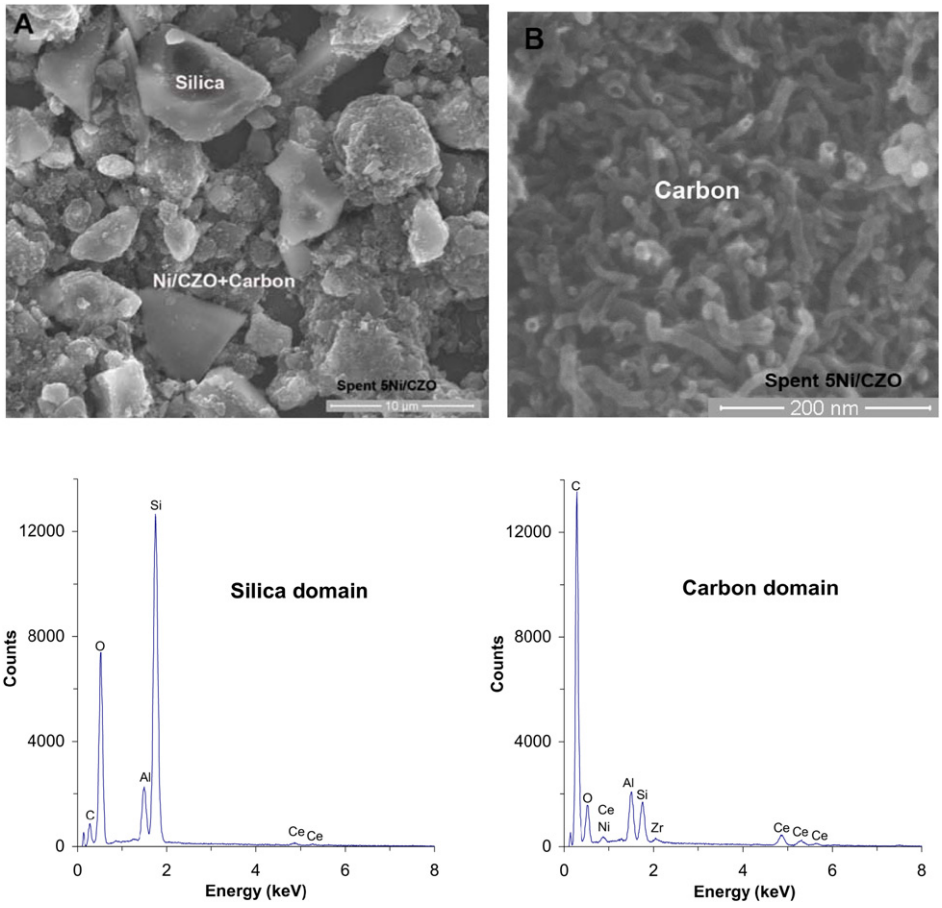

Fig. 10. SEM images and EDS of spent 5Ni/CZO: (A) mixture of Ni/CZO and diluent SiO_2; (B) filamentous carbon domain.

tion on monolith-supported 2% Ni/CZO catalysts gave Ni particle sizes of 21, 27, 33, 37, 50, and 176 nm after 1 h calcination at 600, 700, 800, 900, 1000, and 1100 °C, respectively, proving that the nickel particle size does not change much below 900 °C.

4. Discussion

4.1. Carbon formation on Ni-based catalysts

Carbon formation on Ni-based methane steam-reforming catalysts remains a topic of widespread investigation, with the goal of improving catalyst activity and lifetime. There is scant literature dealing with carbon formation during ATR of heavy feeds; therefore, our discussion is based mainly on results of our work in the context of published results on methane reforming. In general, three types of carbon have been identified on Ni-based steam reforming catalysts: pyrolytic, filamentous, and encapsulating [2,51]. The critical parameters that affect formation of these carbon species include reaction temperature, reactant composition, H_2O/C and/or O/C ratio, and the surface properties of the catalyst. According to Rostrup-Nielsen's review [2] for the formation of different carbon species during catalytic steam reforming, pyrolytic carbon is derived from thermal cracking of the feed hydrocarbons at temperatures above 597 °C with a low H_2O/C ratio over acidic catalysts. Whisker

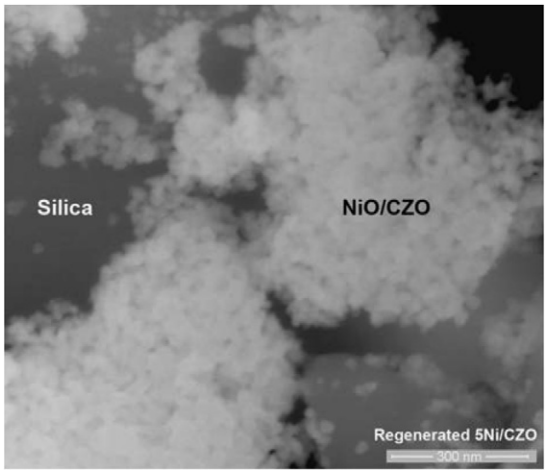

Fig. 11. SEM image of a mixture of regenerated 5Ni/CZO catalyst and diluent SiO_2.

(filamentous) carbon formation occurs at temperatures above 447 °C with a low H_2O/C ratio and aromatic feeds. On nickel catalysts, the structure of filamentous carbon is generally reported as graphitic [17]. Encapsulating carbon is a film of nonreactive deposits that contain C–H bonds and is produced on nickel surfaces through polymerization at temperatures below 497 °C at low H_2O/C ratios and aromatic feeds. The formation of encapsulating carbon results in progressive catalyst deac-

tivation [2]. Alternative pathways, the influence of formation conditions, and a dependence on carbon source have been reported [52–55].

ATR of isooctane is a more complex process than methane steam reforming, not only because it incorporates partial oxidation as well as steam reforming, but also because of the increased complexity of the hydrocarbon structure containing several different C–H and C–C bonds. Both TGA and XPS demonstrated the presence of two types of carbon species in spent catalysts. Combined analysis of TGA, XPS, and SEM clearly showed that coating and filamentous carbon species were formed on Ni/CZO during iC_8-ATR. For the catalysts with nickel loadings $\leqslant 5\%$, both coating and filamentous carbon (nanotubes) were X-ray amorphous. Because IR analysis of the spent catalysts did not show any C–H vibrations, and because no water was evolved during oxidation of the deposited carbon, the lack of C–H bonds in the carbon deposits rules out the possibility of encapsulating carbon. A reasonable explanation for the absence of encapsulating carbon in our catalyst system is that Ce–Zr–O is a weak basic oxide that should prevent hydrocarbons from coking, whereas acidic supports like zeolites facilitate coking [56]. Similarly, recent unpublished TPO/IR experiments on Ni/CZO catalysts have failed to show water evolution from carbon deposited during isooctane decomposition under N_2 atmosphere, or during *n*-dodecane ATR. It is unlikely that the carbon formation is derived purely from thermal pyrolysis of isooctane because no measurable carbon was formed during reaction on SiO_2. If pyrolysis is important, then pyrolytic carbon should have been observed during reaction over SiO_2, because the formation route is homogeneous and independent of the catalyst surface.

The formation of carbon species (coating and filamentous carbon) does not appear to follow the carbon formation mechanism active during methane steam reforming, where the filaments are graphitic and methane decomposition and/or CO disproportionation (Boudouard reaction) are the primary sources of carbon. Filamentous or inactive carbon species were formed from CO disproportionation at high temperatures [57]. Controlled atmosphere electron microscopy has shown that during nickel-catalyzed decomposition of acetylene at 600 °C, amorphous carbon can nucleate around nickel particles and spread over the entire solid [8]. However, it was found that on an alumina-supported nickel methanation catalyst, amorphous carbon (β) is formed at 280 °C [10]. In additional experiments on CZO and 5Ni/CZO used for iC_8 decomposition at 650 °C under N_2 atmosphere, TGA-IR showed only one peak at 280–290 °C for CZO, whereas for 5Ni/CZO two additional peaks were found at temperatures close to those seen after iC_8-ATR. Online IR spectra of the decomposition products indicated the presence of isooctane, isobutene, propylene, and methane. The methane level in the products during iC_8-ATR was <1 mol%, making it unlikely that it acts as a significant carbon source. Based on this, we suggest that carbon formation during iC_8-ATR also involves the participation of low-carbon number alkanes/alkenes ($C \leqslant 4$) that are produced by catalytic cracking of isooctane. In this case, if the breaking of C–H bonds of the cracked smaller molecules is the primary source for deposited carbon, then the H_2 partial pressure in the reactor would be expected to have some effect on carbon deposition. But it is very difficult to isolate the effect of hydrogen partial pressure, because it increases along the fixed-bed integral reactor. Judging from the results, catalysts with different Ni loadings operating under very similar hydrogen partial pressure (Fig. 3B; $H_2O/C = 0.8$) exhibited very different carbon deposition rates (Table 2). Therefore, carbon deposition rates are primarily influenced by Ni loading or nickel particle size.

The low-carbon number alkanes/alkenes ($C \leqslant 4$) observed in the product stream most likely stem from oxidative cracking or dehydrogenation of isooctane. Much work has been done on catalytic cracking of heavy feeds and catalytic oxidative dehydrogenation of light hydrocarbons ($C \leqslant 4$). Unfortunately, very little information exists on the catalytic oxidative cracking [58] and dehydrogenation of isooctane. Two mechanisms account for the cracking of hydrocarbons: the free radical mechanism that is based on the Rice–Kossiakoff theory [59] and the carbonium ion mechanism that deals with catalytic cracking based on surface acidity of catalysts. The oxidative cracking and dehydrogenation of isooctane over a nonacidic Ni/CZO catalyst should follow the free radical type mechanism. Based on recent experiments of dodecane ATR on cordierite monolith-supported Ni/CZO catalysts in our laboratory, we believe that the production of H_2 and CO proceeds through catalytic oxidative cracking and dehydrogenation of large hydrocarbon molecules to C_1–C_4 hydrocarbons, followed by steam reforming of these lighter hydrocarbons [60]. Isooctane has both tertiary and secondary C–C bonds, with primary, secondary, and tertiary C–H bonds. The C–H dissociation energy has the following order: tertiary C–H (381 kJ/mol) < secondary C–H (397 kJ/mol) < primary C–H (410 kJ/mol) < CH_3–H (435 kJ/mol). Applying R–K theory, the probable products of isooctane primary cracking would be isobutene, propylene, methane, hydrogen, and adsorbed carbon. The products of oxidative dehydrogenation would be isobutene, propylene, hydrogen, methane, CO and adsorbed carbon. The adsorbed carbon should be one of the sources of coating carbon. Another source of coating carbon is probably derived from the further cracking or decomposition of low-carbon number alkanes/alkenes ($C \leqslant 4$). It is well known that amorphous carbon is reactive and can be removed by carbon gasification [10,61]. A balance between carbon deposition and gasification is reached on the catalyst. This balance is independent of nickel loading and results in a constant amount of coating carbon as quantified by TGA. In fact, the iC_8 decomposition over 2Ni/CZO showed the formation of a saturation TG curve of weight gain versus the decomposition time on stream in the decomposition temperature range of 400–700 °C.

The mechanism of growth of filamentous carbon is not clearly understood but very likely is quite complex. The carbon for filament formation on Ni/CZO is generated not only by cracking, but also by decomposition of smaller hydrocarbons (alkanes and alkenes) derived from the primary cracking of isooctane or the secondary reactions of the cracked fragments. But the concentrations of these intermediate cracking or decomposition products could not be determined, because these products could not be sampled inside the catalyst bed. Al-

though the formation steps of filamentous carbon are unclear, our results on iC_8 conversion and H_2 yield (Fig. 3) indicated that reaction stages C and D in Fig. 1 were mainly responsible for the deposition of filamentous carbon.

To verify the assumption that most of the carbon deposition occurred during stages C and D, we conducted some additional experiments. iC_8-ATR over 15Ni/CZO catalysts at 500 °C with O/C = 0.5 and $H_2O/C = 1.0$ running for 293 min showed a very low carbon deposition rate of 0.026 g/m^2_{Ni} h. This demonstrates that we can rule out significant carbon deposition at reaction temperatures below 650 °C. When the iC_8-ATR run was repeated over the 5Ni/CZO catalyst using the same protocol shown in Fig. 1 but stopping the reaction after reaching point C, TPO of the catalyst showed a total carbon deposition rate of only 0.060 g/m^2_{Ni} h. This demonstrates that during stages A, B, and C, only small amounts of carbon were deposited, compared with the much higher overall carbon deposition rate of 0.201 $g\,C/m^2_{Ni}$ h obtained when the entire A, B, C, and D protocol of Fig. 1 was executed. These results confirm that the most of the carbon observed postreaction was deposited during stages C and D.

4.2. Carbon deposition and SEM resolution

As demonstrated on the spent 1Ni/CZO sample, the presence of coating carbon deposits reduced surface charging and thus enhanced the SEM image resolution. Fresh NiO/CZO showed poor image resolution compared with the same sample coated with Au. Rather than coating with Au, insulating samples also may be coated with sputtered carbon before SEM analysis to reduce surface charging. In fact, carbon coated onto fresh NiO/CZO via sputtering during SEM sample preparation played a similar role in improving image resolution as the deposited carbon in the post-iC_8-ATR sample. Additional Au coating on this post-iC_8-ATR sample enhanced the SEM image resolution, indicating that the post-ATR coating carbon (T_{392}) still was not sufficient to completely eliminate surface charging.

One remaining question is whether the low-temperature TGA peak is due to coating carbon covering the surface or to the presence of nickel carbide. Ni2p XPS spectra would be useful to identify the presence of carbides. However, even for the nearly carbon-free fresh 2Ni/CZO sample, the nickel signal was very weak. For postreaction samples, no Ni2p XPS peaks were detectable because of carbon deposition on the surface. XRD and TGA provide evidence for ruling out nickel carbides. In TGA, nickel carbides would give rise to a low-temperature peak due to the low thermal stability of nickel carbide [62], and the intensity of this peak should scale with increased nickel loading. But TGA showed that the low-temperature carbon peak remained almost constant in the nickel loading range of 1–15% after iC_8-ATR (Table 2). Furthermore, XRD patterns on spent 15Ni/CZO catalyst showed the presence of metallic nickel with no peaks attributable to carbide (Fig. 2). Thus, the low-temperature carbon peak can be attributed to coating carbon on the surface rather than to carbide.

On catalyst samples with carbon deposits in form of filaments, high-quality SEM images were obtained even without any sputter coating of Au, because the carbon filaments are good electrical conductors. Actually, trying to sputter Au onto these samples proved detrimental, because it damaged the surface morphology of the carbon nanotubes. In addition, higher nickel loading and complete reduction of NiO to metallic nickel were observed to improve SEM imaging.

4.3. Impact of Ni loading

The effect of nickel particle size on the diameter and formation rate of filamentous carbon has received attention for hydrocarbon steam reforming and production of carbon nanotubes and carbon nanofibers. The goal in steam reforming is to inhibit the filament formation rate [17,20], whereas the goal in carbon nanotube and carbon nanofiber production is to enhance the carbon formation rate [19,63]. Studies have shown that the filament diameter is controllable and is very close to the metal particle size [64]. Smaller nickel particles showed resistance to carbon deposition during steam reforming due to the higher saturation concentration of carbon on the nickel particles [19]. Larger nickel particles were found to have a higher carbon deposition rate during methane decomposition [63] and methane [19,38] and butane [20] steam reforming. When nickel size was below a critical level, carbon filament formation or growth did not proceed at all [17,20].

During iC_8-ATR over 1Ni/CZO catalyst with an average nickel particle size of 33 nm, only coating carbon was formed. As the nickel loading doubled to 2%, both coating and filamentous carbon were formed, even though the average nickel particle size remained similar (about 30 nm). Assuming a spherical shape for nickel particles on CZO, the number of nickel particles per unit surface area of CZO would be approximately $1.0 \times 10^{12}/m^2$ for this sample, roughly twice that of the 1% sample. Because the only obvious difference between the 1 and the 2% sample is the number of nickel particles on the support surface, it is conceivable that the growth of filamentous carbon may require not only a critical nickel particle size [17,19,20,63], but also a certain minimum number of nickel particles per unit support area. To better understand the effect of nickel particle size on carbon formation during iC_8-ATR, Fig. 12 summarizes the correlation between nickel particle size and carbon formation rates of both coating as well as filamentous carbon. These rates were estimated by dividing the total amounts of coating and filamentous carbon deposited by the time of stages C and D in Fig. 1, where most of the carbon deposition occurred. The rates of coating carbon formation were low (0.04 g/m^2_{Ni} h) and independent of the nickel particle size; however, the filamentous carbon formation rate increased with nickel particle size. The filamentous carbon formation rate during iC_8-ATR is similar to that found for steam reforming of other hydrocarbons [17,20]. Furthermore, unlike CNT production from a C_1 source (CO or CH_4), no clear correlation was observed between the nickel particle size and the diameter of carbon nanotubes formed during iC_8-ATR over Ni/CZO.

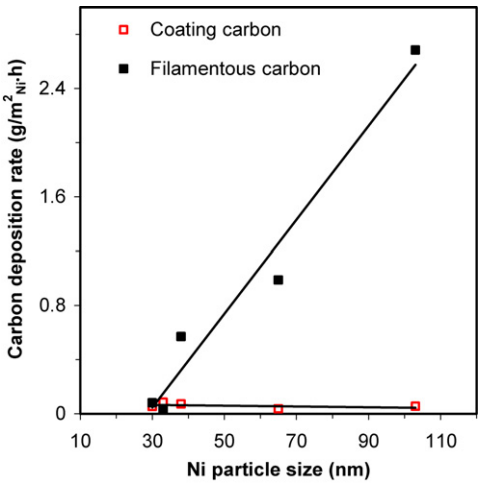

Fig. 12. Correlation between nickel particle size and carbon deposition rate of coating and filamentous carbon.

5. Conclusion

The present work has explored carbon identification and the effects of nickel particle size on carbon formation during iC_8-ATR over Ni/CZO catalysts. Two types of carbon species, coating and filamentous carbon, were characterized by TGA, XRD, XPS, and SEM. The filamentous carbon was present in form of nanotubes, nanofibers, or a mixture of both with diameters of about 12 nm, regardless of nickel particle size. The catalyst with 1% Ni loading demonstrated coating carbon only, whereas catalysts with Ni loading $\geqslant$2% showed both coating and filamentous carbon species. For nickel loadings $\leqslant$5%, both coating and filamentous carbon were X-ray amorphous, even though the deposited carbon reached 60.2 wt%. As the nickel loading was increased to 15%, XRD confirmed the presence of graphite in the deposited carbon. The coating carbon formation rate was low and independent of nickel loading and particle size. The rate of formation of filamentous carbon increased with nickel particle size. The onset of filamentous carbon growth may require a certain minimum number of nickel particles per unit support area. Our findings suggest that during H_2 production from liquid fuels on Ni/CZO catalysts, the growth of filamentous carbon can be inhibited by using small nickel particle sizes and by maintaining a low number of nickel particles per unit support area.

Acknowledgments

Financial support was provided by the US Army Tank-Automotive Research, Development, and Engineering Center (cooperative agreement W56HZV-05-2-0001). The authors thank the Electron Microbeam Analysis Laboratories (EMAL) of the University of Michigan for providing access to the XPS and SEM instruments and Tom Westrich for engaging in useful discussions regarding the thermal decomposition of isooctane.

Supplementary material

Supplementary material for this article may be found on ScienceDirect, in the online version.

Please visit DOI: 10.1016/j.jcat.2007.07.031.

References

[1] S. Jain, H.-Y. Chen, J. Schwank, J. Power Sources 160 (2006) 474.
[2] J.R. Rostrup-Nielsen, in: J.R. Anderson, M. Boudart (Eds.), Catalysis: Science and Technology, Chapter 1: Catalytic Steam Reforming, Springer-Verlag, New York, 1984, p. 30.
[3] F.J. Dent, L.A. Moignard, A.H. Eastwood, W.H. Blackbum, Trans. Inst. Gas Eng. (1945–1946) 602.
[4] J.R. Rostrup-Nielsen, J. Catal. 27 (1972) 343.
[5] R.T.K. Baker, Catal. Rev. Sci. Eng. 19 (1979) 161.
[6] D.L. Trimm, Catal. Rev. Sci. Eng. 16 (1977) 155.
[7] J.R. Rostrup-Nielsen, D.L. Trimm, J. Catal. 48 (1977) 155.
[8] R.T.K. Baker, D.J.C. Yates, J.A. Dumesic, in: L.F. Albright, R.T.K. Baker (Eds.), Coke Formation on Metal Surfaces, in: ACS Symposium Series, vol. 202, Am. Chem. Soc., Washington, DC, 1982, p. 177.
[9] C.H. Bartholomew, Catal. Rev. Sci. Eng. 24 (1982) 67.
[10] J.G. McCarty, H. Wise, J. Catal. 57 (1979) 406.
[11] R.T.K. Baker, M.A. Barber, P.S. Harris, F.S. Feates, R.J. Waite, J. Catal. 26 (1972) 51.
[12] T. Zhang, M.D. Amiridis, Appl. Catal. A 167 (1998) 161.
[13] I. Alstrup, J. Catal. 109 (1988) 241.
[14] K.P. De Jong, J.W. Geus, Catal. Rev. Sci. Eng. 42 (2000) 481.
[15] S. Helveg, C. López-Cartes, J. Sehested, P.L. Hansen, B.S. Clausen, J.R. Rostrup-Nielsen, F. Abild-Pedersen, J.K. Nørskov, Nature 427 (2004) 426.
[16] F. Abild-Pedersen, J.K. Nørskov, J.R. Rostrup-Nielsen, J. Sehested, S. Helveg, Phys. Rev. 73 (2006) 115419.
[17] H.S. Bengaard, J.K. Nørskov, J. Sehested, B.S. Clausen, L.P. Nielsen, A.M. Molenbroek, J.R. Rostrup-Nielsen, J. Catal. 209 (2002) 365.
[18] L.H. Liang, F. Liu, D.X. Shi, W.M. Liu, X.C. Xie, H.J. Gao, Phys. Rev. B 72 (2005) 035453.
[19] K.O. Christensen, D. Chen, R. Lødeng, A. Holmen, Appl. Catal. A 314 (2006) 9.
[20] T. Borowiecki, Appl. Catal. 4 (1982) 223.
[21] D.L. Trimm, Catal. Today 49 (1999) 3–10.
[22] C.A. Bernardo, I. Alstrup, J.R. Rostrup-Nielsen, J. Catal. 96 (1985) 517.
[23] I. Alstrup, M.T. Tavares, J. Catal. 139 (1993) 513.
[24] P.M. Holmblad, J.H. Larsen, I. Chorkendorff, L.P. Nielsen, F. Besenbacher, I. Stensgaard, E. Lægsgaard, P. Kratzer, B. Hammer, J.K. Nørskov, Catal. Lett. 40 (1996) 131.
[25] F. Besenbacher, I. Chorkendorff, B.S. Clausen, B. Hammer, A.M. Molenbroek, J.K. Nørskov, I. Stensgaard, Science 279 (1998) 1913.
[26] E. Nikolla, A. Holewinski, J. Schwank, S. Linic, J. Am. Chem. Soc. 128 (2006) 11354.
[27] J. Xu, M. Saeys, J. Catal. 242 (2006) 217.
[28] T. Borowiecki, A. Gołębiowski, Catal. Lett. 25 (1994) 309.
[29] T. Borowiecki, A. Gołębiowski, B. Stasińska, Appl. Catal. A 153 (1997) 141.
[30] J.R. Rostrup-Nielsen, J. Catal. 85 (1984) 31.
[31] C.A. Bernardo, I. Alstrup, J.R. Rostrup-Nielsen, J. Catal. 96 (1985) 517.
[32] S.P.S. Andrew, Ind. Eng. Chem. Prod. Res. Dev. 8 (1969) 321.
[33] T. Horiuchi, K. Sakuma, T. Fukui, Y. Kubo, T. Osaki, T. Mori, Appl. Catal. A 144 (1996) 111.
[34] Q. Miao, G. Xiong, S. Sheng, W. Cui, L. Xu, X. Guo, Appl. Catal. A 154 (1997) 17.
[35] D.L. Trimm, A.A. Adesina, Praharso, N.W. Cant, Catal. Today 93–95 (2004) 17.
[36] L. Pino, A. Vita, F. Cipitì, M. Laganà, V. Recupero, Appl. Catal. A 306 (2006) 68.
[37] G. Liu, F. Qiu, S. Guo, Cuihua Xuebao 11 (1990) 45.
[38] Q. Zhuang, Y. Qin, L. Chang, Appl. Catal. 70 (1991) 1.

[39] K. Tomishige, T. Kimura, J. Nishikawa, T. Miyazawa, K. Kunimori, Catal. Commun. 8 (2007) 1074.
[40] P. Ferreira-Aparicio, M.J. Benito, Ind. Eng. Chem. Res. 44 (2005) 742.
[41] A. Shamsi, J.P. Baltrus, J.J. Spivey, Appl. Catal. A 293 (2005) 145.
[42] S. Specchia, A. Cutillo, G. Saracco, V. Specchia, Ind. Eng. Chem. Res. 45 (2006) 5298.
[43] B.F. Hagh, J. Power Sources 130 (2004) 85.
[44] L. Villegas, N. Guilhaume, H. Provendier, C. Daniel, F. Masset, C. Mirodatos, Appl. Catal. A 281 (2005) 75.
[45] A.R. Tadd, B.D. Gould, J.W. Schwank, Catal. Today 110 (2005) 68.
[46] P.K. Cheekatamarla, A.M. Lane, J. Power Sources 152 (2005) 256.
[47] M. Pacheco, J. Sirge, J. Kopasz, Appl. Catal. A 250 (2003) 161.
[48] F. Pompeo, N.N. Nichio, O.A. Ferretti, D. Resasco, Int. J. Hydrogen Energy 30 (2005) 1399.
[49] B.D. Gould, A.R. Tadd, J.W. Schwank, J. Power Sources 164 (2007) 344.
[50] A. Tadd, Ph.D. dissertation, The University of Michigan, 2006.
[51] J. Sehested, Catal. Today 111 (2006) 103.
[52] P.E. Nolan, D.C. Lynch, A.H. Cutler, J. Phys. Chem. B 102 (1998) 4165.
[53] T. Baird, J.R. Fryer, B. Grant, Carbon 12 (1974) 591.
[54] G.G. Kuvshinov, Yu.I. Mogilnykh, D.G. Kuvshinov, D.Yu. Yermakov, M.A. Yermakova, A.N. Salanov, N.A. Rudina, Carbon 37 (1999) 1239.
[55] N.A. Kiselev, A.V. Krestinin, A.V. Raevskii, O.M. Zhigalina, G.I. Zvereva, M.B. Kislov, V.V. Artemov, Yu.V. Grigoriev, J.L. Hutchison, Carbon 44 (2006) 2289.
[56] A.A. Brillis, G. Manos, Ind. Eng. Chem. Res. 42 (2003) 2292.
[57] D.W. Goodman, R.D. Kelley, T.E. Madey, J.T. Yates Jr., J. Catal. 64 (1980) 479.
[58] X. Liu, W. Li, H. Zhu, Q. Ge, Y. Chen, H. Xu, Catal. Lett. 94 (2004) 31.
[59] A. Kossiakoff, F.O. Rice, J. Am. Chem. Soc. 65 (1943) 590.
[60] B.D. Gould, X. Chen, J.W. Schwank, J. Catal. (2007), doi:10.1016/j.jcat.2007.06.020.
[61] T.V. Choudhary, D.W. Goodman, Catal. Lett. 59 (1999) 93.
[62] S. Nagakura, J. Phys. Soc. Jpn. 12 (1957) 482.
[63] D. Chen, K.O. Christensen, E. Ochoa-Fernández, Z. Yu, B. Tøtdal, N. Latorre, A. Monzón, A. Holmen, J. Catal. 229 (2005) 82.
[64] C.L. Cheung, A. Kurtz, H. Park, C.M. Lieber, J. Phys. Chem. B 106 (2002) 2429.